Check for updates

ORIGINAL ARTICLE

Bikash Mahato · Saurabh Saxena · Neda Yaghoobian

Aerodynamic force modifications of a spherical particle with varying temperature: a study of an idealized firebrand

Received: 10 November 2023 / Accepted: 5 May 2024 © The Author(s), under exclusive licence to Springer-Verlag GmbH Germany, part of Springer Nature 2024

Abstract Fully resolved direct numerical simulations are used to quantify the effect of evolving heat, due to idealized smoldering processes, on the aerodynamic forces of a spherical particle, representing an idealized fixed-shape firebrand particle. Firebrand particles are small glowing particles that are generated in fires and can be transferred long distances by the wind and create new spot fires. Understanding the transport of firebrands is of great importance in fire science. The simulations are performed at a Reynolds number of 500, relevant for a wide range of firebrand size and wind velocity combinations. The spatiotemporal variation of temperature over the surface of the particle is obtained using a detailed surface energy balance analysis. The firebrand particle is assumed to have the thermal and material properties of pine needles and has a Biot number larger than unity, which means that the particle undergoes notable internal temperature gradients. The results indicate that the buoyancy-induced flow around the particle significantly modifies the trailing vortices and produces two non-interacting tunnel-shaped plumes in the wake of the sphere as the particle's Richardson number increases. As a result, the particle's drag and lift coefficients show large deviations from those of a non-heated particle and an isothermal particle. The increased surface temperatures result in an increase in the drag force while inducing a negative lift. The significant variations seen in the aerodynamic forces as a function of the particle's instantaneous temperature indicate that the influence of the transient thermal conditions of firebrands should be considered in the prediction of the particles' trajectory and landing spots.

 $\textbf{Keywords} \quad \text{Buoyancy effect} \cdot \text{Crossflow mixed convection} \cdot \text{DNS} \cdot \text{Instantaneous temperature} \cdot \text{Particle trajectory} \cdot \text{Smoldering particle} \cdot \text{Vortex}$

1 Introduction

Wildfires are natural or man-created problems that are growing in the United States and around the world. According to the U.S. National Interagency Coordination Center [33], 72,000 wildfires are reported on average each year in the United States, leading to the burning of over 5 million acres of land and resulting in around 4000 deaths annually. The U.S. Forest Service and the Department of Interior reportedly spend over 2 billion dollars per year to suppress and control wildfires [33]. Wildfire problems become even more serious when the fire spreads into communities and creates wildland-urban interface (WUI) fires [23–25,53,59]. In wildfires, fragments of burning materials, known as firebrands (or flying embers) are generated, lofted, and carried by the wind several meters to kilometers ahead of the main fire-front and create several new spot fires [e.g., 19,47,48,59]. Post-fire studies indicate that firebrands are responsible for the fastest spread and the majority

Communicated by Atul Sharma.

Bikash Mahato · Saurabh Saxena · Neda Yaghoobian (⊠)
Department of Mechanical Engineering, FAMU-FSU College of Engineering, Florida State University, Tallahassee, FL, USA E-mail: nyaghoobian@eng.famu.fsu.edu

Published online: 30 May 2024

of the ignitions, especially, in WUI areas [e.g., 9,24,27,55,56]. Investigating the different mechanisms in the transport of firebrand particles is an important step in understanding the spotting phenomenon, which helps in a better risk assessment and improved mitigation methods.

Like any other projectile, the transport of firebrand particles is controlled by the gravitational and aerodynamic forces exerted on the particles and depends on the particle attributes and the local wind characteristics. The transport of firebrands has been investigated in several experimental and computational studies. For example, in the early work of Tarifa et al. [50,51], the influence of firebrand shape, size, moisture, and density on the spotting distance of firebrands was experimentally investigated and the burning time, flight path, and aerodynamic forces on the firebrand particles for a uniform wind condition was determined. In these studies, however, a correlation that relates the aerodynamic forces to the firebrand attributes and particularly to the particle temperature was not provided. Later, Albini [2-4] used the findings of Tarifa et al. [50,51] and investigated the spotting distance of cylindrical-shaped firebrands, under the lofting effect of buoyant plumes, using a constant drag coefficient. In the work of Tse and Fernandez-Pello [58] the flight paths of hot spherical copper and aluminum particles were investigated numerically, for which a modified Stoke's drag coefficient relation for a non-heated sphere was used to predict the aerodynamic forces on the particles. The work of Tse and Fernandez-Pello [58] was further extended by Anthenien et al. [5] to investigate the flight path of particles with spherical, cylindrical, and disk shapes. In this study, for a better prediction of the flight trajectories, Anthenien et al. [5] applied a drag coefficient relation based on Clift and Gauvin [12] that uses an extended range of Reynolds numbers (Re). In the work of Bhutia et al. [9], the effect of the background atmospheric boundary layer turbulence was investigated on the three-dimensional (3D) trajectory of combusting and non-combusting spherical firebrands using a constant drag coefficient of 0.45 which is assumed to be a good approximation for a wide range of Re. Pereira et al. [37] investigated the effect of turbulent wind in and over vegetation and idealized forest fire on the maximum spotting distance of combusting spherical particles, in which the drag coefficient they considered [43], similar to the other aforementioned studies, was a function of particle Re only, assuming that the fluid is uniformly at the same temperature. Given that the particle's instantaneous temperature may alter the near-surface velocity field, it is expected that the aerodynamic forces on firebrand particles constantly change as the particle undergoes the smoldering (or burning) process. Previous fundamental studies (e.g., Oppenheimer et al. [35], Ganguli and Lele [14], Wang et al. [63], and Kurose et al. [21]) have in fact shown that for a wide range of particle temperature and Re, in variable or non-variable property flows, the drag coefficient of particles is affected and increases by the particle temperature. Nevertheless, to our best knowledge, the aerodynamic forces on the firebrand particles in relevant literature are treated independent of the particle temperature and fundamental studies on spherical particle aerodynamics lack information on the effect of the unsteady spatiotemporal variations of particle temperature.

This study aims to investigate the effects of evolving temperature of a sphere (representing an idealized smoldering firebrand) on its instantaneous aerodynamic forces, which define the particle trajectory. The spatiotemporal evolution of firebrand temperature is estimated using energy balance analysis and an idealized smoldering process for a particular material. The simulated surface temperatures are then used as a spatiotemporally variable thermal boundary condition for a direct numerical simulation (DNS) to predict the flow behavior over the sphere. Based on the particle maximum film temperature (i.e., the average of the particle maximum surface temperature and free-stream temperature), the change in the fluid density is small ($\Delta \rho/\rho \ll 1$), making the use of the Boussinesq approximation valid (e.g., Burmeister [10]). The rest of the paper explains the details of the study and its findings. The models used in this work and the simulation set-up are presented in Sect. 2. Results and discussions are provided in Sect. 3, followed by the conclusion in Sect. 4.

2 Model description and simulation set-up

2.1 Model description

The simulations were performed using a DNS-based model with a sharp interface immersed boundary method [30]. The Navier-Stokes and the thermal convection equations (see Appendix A) are discretized using a finite difference method and a cell-centered, collocated arrangement of velocity, pressure, and temperature. Face-center velocities are also computed, in addition to the cell-centered ones, to impose the incompressibility constraint and ensure a strong coupling between the velocity and pressure [64,66]. The equations are integrated in time using the fraction step method [11,60,66]. A second-order Crank-Nicholson scheme is employed to discretize the momentum equation and a second-order central difference scheme is used for the spatial derivatives, while the pressure Poisson equation is solved using a bi-conjugate gradient method with stabilization.

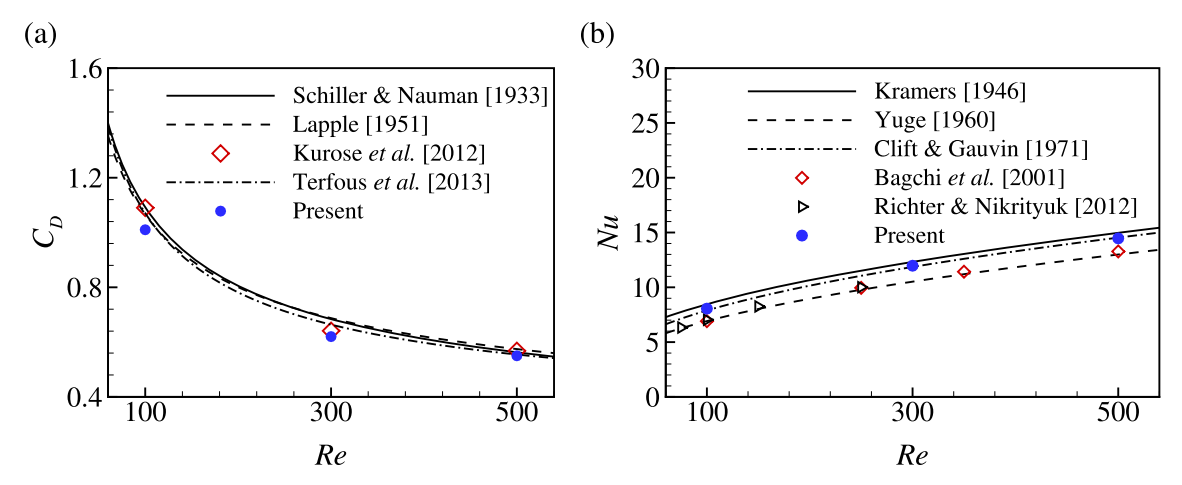


Fig. 1 Validation of the present numerical method for different Re, showing the time-averaged drag coefficient (C_D) comparison for a non-heated sphere (a), and Nusselt number (Nu) comparison for a uniformly heated sphere (b)

The surface of the immersed boundary is represented by an unstructured mesh with triangular elements. For this study, transient spatiotemporally variable thermal boundary conditions were implemented by setting each triangular mesh element of the immersed boundary surface to specified precalculated temperatures that vary with time (explained later below and in Appendix A).

The accuracy of the DNS-based model has previously been validated for a wide range of complex fluid flow problems [e.g., 13,30,46,61,67]. Here, the performance of the model was investigated against the correlations found by Lapple [22], Schiller and Nauman [43], and Terfous et al. [52] and the numerical work of Kurose et al. [21] for the drag coefficient of a non-heated sphere. In addition, the performance of the model for predicting the Nusselt number of an isothermal sphere was investigated against the empirical correlations of Clift and Gauvin [12], Kramers [20], and Yuge [65] and numerical works of Bagchi et al. [6], and Richter and Nikrityuk [40] for forced convection flows. Kramers [20], and Yuge [65] reported correlations from their experimental observations, whereas Clift and Gauvin [12] developed a correlation by combining previous experimental observation data to cover a wide Re range. These validation studies were performed for three Re of 100, 300, and 500 based on the diameter of the sphere, and the results are shown in Fig. 1. Figure 1a compares the simulated time-averaged drag coefficients (C_D) for a non-heated sphere and Fig. 1b compares the Nusselt number (Nu) for a uniformly heated sphere against the correlations from the literature, both showing very good agreements. C_D and Nu were calculated according to Eqs. (1) and (2), respectively.

$$C_D = \frac{1}{\frac{1}{2}\rho U_{\infty}^2 A} \left(-\int_S p\mathbf{e_x} \cdot \mathbf{n} \, dS + \int_S \mathbf{n} \cdot \boldsymbol{\tau} \cdot \mathbf{e_x} dS \right) \tag{1}$$

$$Nu = \frac{D}{(T_S - T_\infty) S_0} \int_S \left(-\frac{\partial T}{\partial r} \Big|_{r=D} dS \right)$$
 (2)

In these equations, A and D are, respectively, the projected area and diameter of the sphere. $\mathbf{e_x}$ and \mathbf{n} are the x-component unit vector and surface unit normal, respectively, p is the pressure, ρ is the density of the air, U_{∞} is the freestream velocity, S_0 is the surface area of the sphere, T is the temperature, with subscripts s and ∞ representing the sphere surface and the far-field flow, respectively. τ and r are the viscous stress tensor and radial distance, respectively. In addition to the above validation studies, the model's performance in predicting the Nusselt numbers of an isothermal sphere under crossflow mixed-convection conditions was assessed. In this regard, two cases with Richardson numbers (Ri, defined later) of 0.0567 and 1.0 at Re = 100 were examined. These Richardson numbers are in the same Ri range as those considered in this study. The model predicts time averaged Nusselt numbers of 7.08 (Ri = 0.0567) and 7.997 (Ri = 1.0) for these cases. These findings were compared against experimental data of Yuge [65] and Musong and Feng [31]. Yuge [65] reported a Nusselt number of 7.02 for Ri = 0.0567, while Musong and Feng [31] reported Nusselt number values of 6.94 and 7.924 for Ri = 0.0567 and 1.0, respectively. The Nusselt number simulated by the model agrees within a 2% relative deviation with the literature values for both Ri.

As mentioned earlier, the thermal boundary condition over the sphere was simulated using surface energy balance analysis to impose a transient thermal state on the particle's surface. The surface energy balance modeling is performed using the Complex-environment Temperature and Moisture Predictor (CeTMP) model that simulates the spatiotemporally variable temperature and dryness of 3D objects/fuels with complex shapes and material settings under diurnally variable open-atmosphere environmental conditions. CeTMP considers all the relevant energy exchange terms in the surface energy budget calculations, i.e., shortwave and longwave radiations, conduction, and convection heat transfers to calculate surface temperatures in high spatial resolution across different time scales. Each surface unit (patch) is in instantaneous energy exchange with its local environment and the surrounding patches/objects. The CeTMP model formulations relevant to the present work are presented in Appendix A. Complete details of the model and its validation can be found in Saxena et al. [42]. In this work, CeTMP was used to simulate the spatiotemporally variable surface temperature of a sphere under the effect of an internal transient smoldering heat source and an external variable velocity field over the surface of the sphere. The patch-resolved temporally variable surface temperatures obtained from CeTMP were then employed as the transient thermal boundary conditions for each patch of the sphere in the DNS simulations. The one-way coupling of the two numerical models (explained in Appendix A) allows for the investigation of the aerothermodynamic behavior of a spherical particle with an internal transient heat source, representing an idealized (smoldering) firebrand.

2.2 Simulation set-up

A rectangular computational domain of size 24D (streamwise) $\times 10D$ (spanwise) $\times 10D$ (vertical) was considered for the simulations. This domain size was found through sensitivity analysis and its length is long enough for flow perturbations to decay far from the sphere. In the spanwise, vertical, and upstream directions, under no-heat conditions, the flow perturbations created due to the presence of a sphere decay away at a rate of $1/r^3$ [8], with r being the radial distance measured from the sphere center, which results in a velocity with less than 0.1% difference from the free-stream velocity at r > 5D [57]. Our domain sensitivity study using a heated sphere indicates that the aerodynamic forces are unaffected by the side and upstream boundaries, when the above criterion is satisfied. In addition, the effective blockage (area) ratio, defined as the ratio of the sphere's frontal area and computational domain's frontal area, is 0.08%, which is < 0.1% and, hence, is within an acceptable range [1,17]. A total of $248 \times 197 \times 197$ non-uniform grid points were placed inside the computational domain with a higher grid point density close to the sphere. The minimum grid spacing near the sphere surface was found based on a grid sensitivity analysis and the boundary layer thickness at the front stagnation point of the sphere. This thickness was approximated at $\delta = 1.13/\sqrt{Re}$ [44], where, δ is the non-dimensional boundary layer thickness based on the sphere diameter. At least ten grid points were placed within the boundary layer, resulting in a minimum non-dimensional grid spacing of $\Delta_{min} = 1.13/(10 \times \sqrt{Re})$ near the sphere surface [16]. The considered grid spacing is sufficient to capture the physics of the smallest eddies as the minimum grid size is smaller than the Kolmogorov length scale of the flow, $\eta = D/Re^{3/4}$ [39] = 0.009. A coarser computational grid distribution was used far from the sphere to reduce the computational cost. The grid stretching factor was considered less than 1.06 to avoid numerical instabilities. The details of the domain and grid independency analyses are included in Appendix B. No-slip, no-penetration velocity boundary conditions, and Dirichlet thermal boundary conditions were applied on the surface of the sphere. Neumann, zero-gradient, velocity boundary condition was considered for the outer boundaries except for the inlet, which uses a Dirichlet boundary condition of a uniform horizontal flow. Neumann zero-gradient boundary condition was applied for pressure on the external boundaries. The domain attributes, boundary conditions, and the position of the sphere in the domain are shown in Fig. 2.

In nature, the firebrand size and the background flow velocity can vary significantly in different fire scenarios. According to the literature, the size of firebrands can vary from a few millimeters [62] to a few centimeters [34], while the background wind velocity was observed to range from 3 m/s and less [49] to 12 m/s [45] in wildfire zones. The *Re* of the idealized firebrand particle in this study was chosen 500, which covers a wide range of firebrand size and wind velocity combinations, while allows for manageable computational expenses.

The Dirichlet thermal boundary condition over the firebrand is a spatiotemporally variable surface temperature found through surface energy balance analysis in CeTMP. For this analysis, we assumed that the firebrand possesses the material and thermal properties characteristic of pine needles, commonly encountered as firebrand materials in wildfires. These specifics are outlined in Table 1.

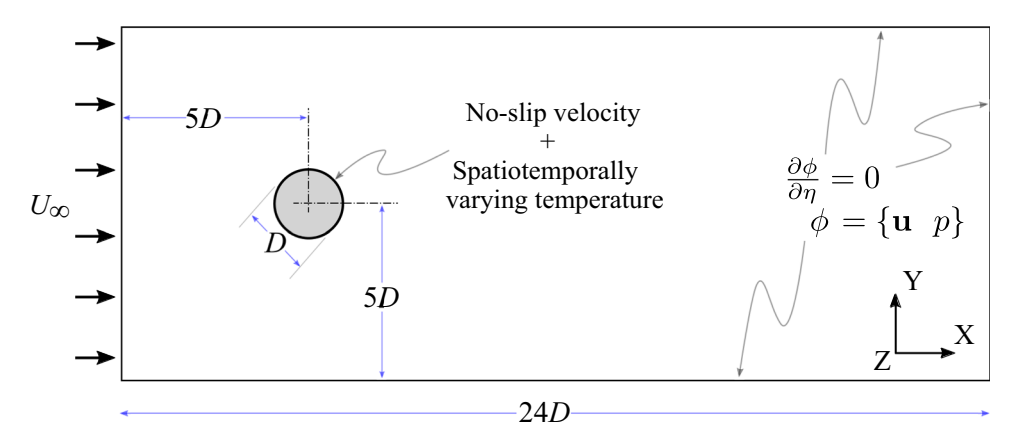


Fig. 2 Schematic of the computational domain (not to scale)

Table 1 Thermal and material properties of the firebrand based on the properties of Pine needles

Fuel type	Density (kg m ⁻³)	Heat capacity (J g ⁻¹ K ⁻¹)	Ignition temperature (K)	Conductivity (W m ⁻¹ K ⁻¹)	Emissivity	Material thickness (m)
Pine needles	615.3 ^a	1470 ^b	549 ^c	0.12 ^d	0.8646	0.025

^aRivera et al. [41]

The firebrand particle surface in CeTMP was divided into equilateral triangular patches and a uniform material was considered within the particle. The innermost layer of the particle was subjected to internal heat with a variation following the general trend of the heat release rate in the t^2 -fire growth model [18]. The t^2 -fire growth model represents heat release rates of typical burning items versus time, determining the time taken for a material to reach the maximum heat release rate, the time to start heat release decay, and the end time of heat release (see Appendix A). Following this trend, the resulting temperature evolution inside the particle's internal layer signifies that the material reaches a level-off or smoldering state and remains in this state for a certain period, following which it decays to an extinguishing point. This temperature profile represents the internal temporally varying thermal boundary condition for each patch on the surface of the firebrand in the energy balance analysis. Due to the complexity of detailed combustion models and the absence of simple smoldering models, the t^2 -fire growth model [18] was adopted to estimate the temperature variation of an idealized firebrand.

On the surface of each patch, the heat convection process is dependent on the patch's local wind velocity and the patch surface and ambient air temperatures. The McAdams [26,36] convective coefficient correlation was employed to estimate the convective coefficient at each patch surface as a function of local velocities, for which the local wind velocities were found from DNS of the flow past a non-heated sphere at Re = 500. The ambient air temperature was set to the film temperature of 349.15 K (76 °C) based on the maximum surface temperature of the sphere and a free-stream temperature (T_{∞}) of 298.15 K (25 °C). Figure 3 shows temporal variations of the normalized spatially averaged surface temperature of the sphere. This surface temperature evolution follows the trend of the internal smoldering heat release that reaches and remains at a maximum surface temperature for a certain period and then cools down. The normalized maximum local temperature deviation from the mean temperature on the sphere surface at an instant ($T_{s,max} - T_{s,avg}/T_{\infty}$), which is a result of the variation of the flow velocity at the sphere surface, is around 9% throughout the smoldering process. The normalized instantaneous surface temperature distribution at the maximum temperature instant is shown in Fig. 4. The instantaneous surface temperature distribution inversely follows the near-surface velocity distribution (not shown), with the surface in the wake region of the sphere bearing higher temperatures owing to the lower velocities.

Given the explained setup, the average Biot number of the sphere is in the range of 3.4, which indicates a considerable variation and sustained gradient of temperature inside the body. The explained model setup provides a one-way coupled framework between the DNS and energy balance analysis that allows for investigating

^bGrishin [15]

^cMindykowski et al. [28]

^dBaranovskiy and Malinin [7]

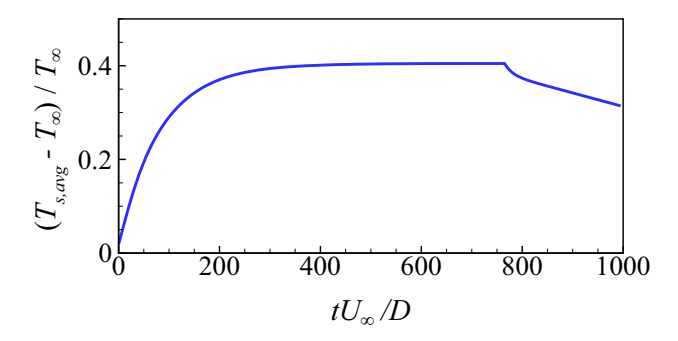


Fig. 3 Time variation of the normalized spatially averaged surface temperature of the spherical firebrand found from energy balance analysis

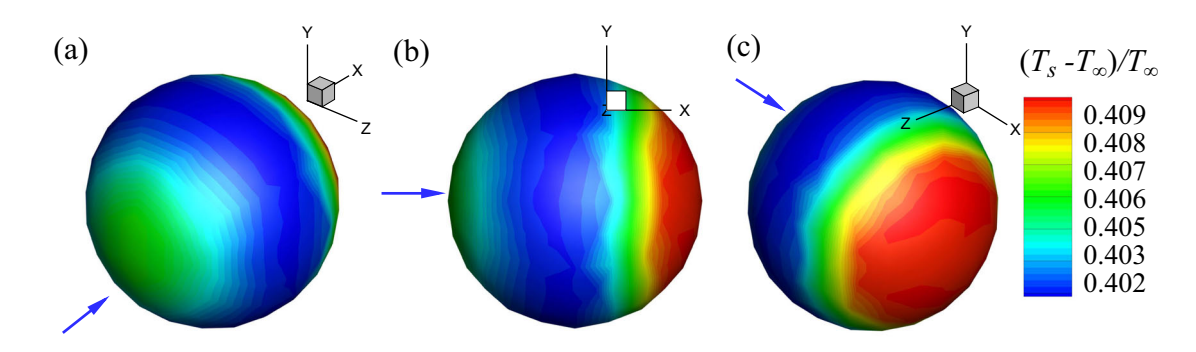


Fig. 4 Instantaneous normalized surface temperature distribution at the maximum temperature. The different panels show the temperature distributions from various views. The blue arrow indicates the wind direction

the flow features over a sphere that is heated nonuniformly according to the spatial variation of the near-surface wind profile. Based on the calculated film temperature, the density variation of the flow is small ($\Delta \rho/\rho = 0.15$), and therefore the use of the Boussinesq approximation is applicable. Also, based on the film temperature, the viscosity variation within the convection boundary layer is small ($\Delta \mu/\mu = 0.11$) and therefore negligible. In this study, it is assumed that the firebrand conserves its shape as it goes through the smoldering process and only the effect of the unsteady smoldering heat on the aerodynamic forces was investigated under Re = 500.

3 Results and discussions

3.1 Observation of the wake flow behavior

Characteristics of the flow passing over non-heated spheres under different Re have been investigated previously [e.g., 16,29,32,38,54,57]. In this section, the instantaneous Q-criterion of the flow over a non-heated sphere at Re = 500 is provided as a reference (Fig. 5). The instantaneous second invariant of the velocity gradient tensor (Q-criterion) defines vortices as regions where the vorticity magnitude exceeds the magnitude of the rate of strain. Q-criterion is calculated as $Q = \frac{1}{2} (\|\Omega\|^2 - \|\mathbf{S}\|^2)$, where Ω is the vorticity vector and \mathbf{S} is the strain rate tensor. Regions with Q > 0 signify the presence of vortices. Figure 5a and b, respectively, show the side and top views of the instantaneous wake vortex structures. The interlocked hairpin vortices that are advected downstream and are aligned with the direction of the freestream flow are observed.

Figure 6 shows the distribution of the time-averaged coefficient of pressure $\left(C_p = (p-p_\infty)/\frac{1}{2}\rho U_\infty^2\right)$ along the vertical (z) and horizontal (y) cross-sectional planes of the same non-heated sphere. As expected, although the instantaneous unsteady flow field represents asymmetric patterns behind the sphere (due to the alternating vortex formations in the sphere wake), the time-averaged pressure coefficient reflects the axisymmetric nature of the fully developed flow field due to the generation of similar structures at the same locations.

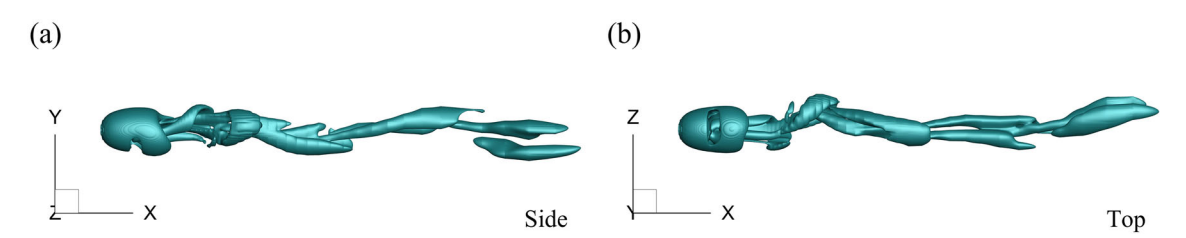


Fig. 5 Instantaneous Q-criterion (Q = 0.01) iso-surfaces of the flow behind a non-heated sphere at Re = 500 viewed from the a side and b top directions

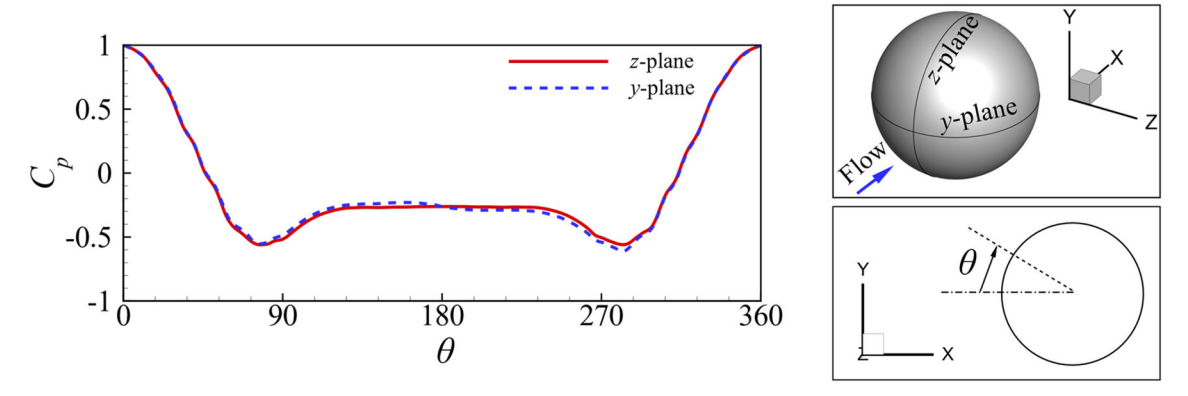


Fig. 6 Time-averaged pressure coefficient (C_p) on the surface of a non-heated sphere at Re = 500 along the y- and z-planes. Inset images show the orientation of the y- and z-planes, and the angle (θ) is measured from the front of the sphere

Since, in this study, the temperature of the sphere is temporally variable and at the same time the sphere is subjected to external flows, the problem may involve both natural and forced convection modes of heat transfer depending on the particle's instantaneous temperature. To determine the relative importance of each mode of heat transfer and to investigate how these modes impact the aerodynamic behavior of the sphere, the dimensionless Richardson number was used. Richardson number is defined as $Ri = Gr/Re^2 = g\beta \left(T_{s,avg} - T_{air}\right) D/U_{\infty}^2$, where Gr is the Grashof number, g is the gravitational acceleration, β is the thermal expansion coefficient (= $1/T_{s,avg}$, where $T_{s,avg}$ is the spatially averaged surface temperature of the sphere at an instant), and T_{air} is the ambient temperature that is considered the average of the maximum surface temperature of the sphere and the far-field temperature. $Ri \ll 1$ signifies that the flow is dominated by forced convection, $Ri \gg 1$ indicates that the flow is natural convection dominated, and with $Ri \approx 1$, both inertia and buoyancy forces are equally important, and thus the flow is mixed convection.

In the present simulations of the flow past an idealized firebrand particle, Ri varies following the variations in the particle smoldering heat input and the sphere surface temperature (as shown with a red solid line in Fig. 7). The Ri value is small initially when the particle surface temperature is close to the ambient temperature and then it increases until the smoldering heat (and Ri) start decaying at $\hat{t} = tU_{\infty}/D = 760$.

The inset images in Fig. 7 show the side view of the wake vortices Q-criterion behind the sphere as it goes through the temperature variations. It can be noticed that the flow characteristics develop from forced convection in the initial stages of the simulation and gradually shifts to the mixed convection regime. The vertical shifting of the wake vortices in higher Ri is a consequence of continuously increasing sphere surface temperature and the larger buoyancy effects. A noticeable characteristic of the wake flow is that the interlocking hairpin vortex structures behind the sphere, which appear under the no-heat condition, gradually vanish and merge to form two well-defined tunnel-shaped heat plumes behind the sphere (see Fig. 8 below) as the Ri increases. The fully formed tunnel-shaped heat plumes are detected at Ri > 0.7. To emphasize the variations in the vertical orientation of the trailing vortices at different stages, a dotted vertical reference line is shown at the top right corner of the insert images for Ri larger than 0.7.

Similar to the variation trend of the Ri, the spatially averaged Nusselt number on the surface of the sphere varies (not shown) following the same variation trend of the sphere surface temperature and the particle smoldering heat input, indicating that the convection mode dominates the conduction mode in the fluid as the sphere temperature increases. The magnitude of the Nusselt number varies between the range of 0-21

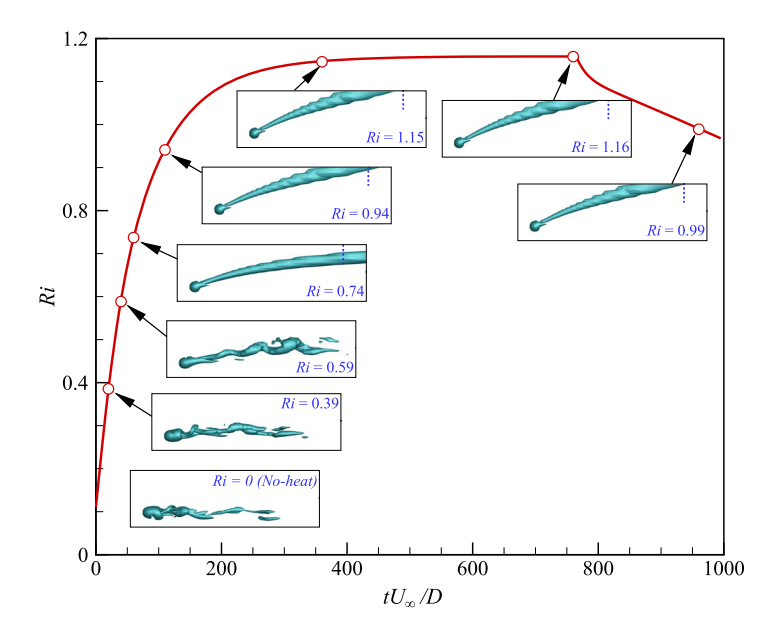


Fig. 7 Temporal variations of the Richardson number (Ri) associated with the flow over an idealized smoldering particle. The insert figures show Q-criterions (Q = 0.02) of the particle wake flow at different instances of the smoldering heat variation

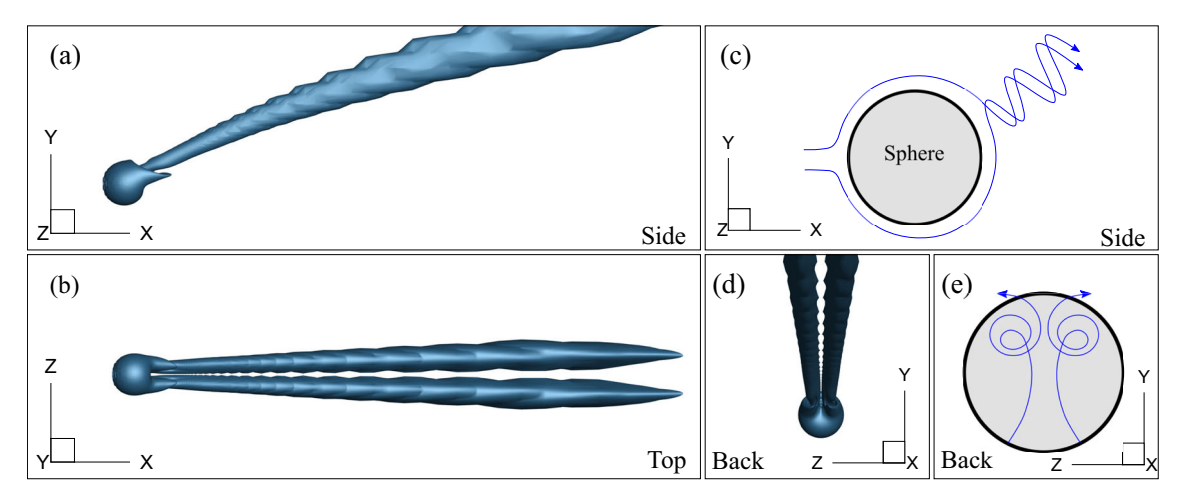


Fig. 8 Side (a), top (b), and back (d) views of the instantaneous Q-criterion (Q = 0.05) of a mixed-convection flow at Ri = 0.94. Subplots (c) and (e), respectively, represent schematics of the flow streamlines from the side and back views

and reaches the maximum value at around $\hat{t}=760$. One can notice that the Nusselt number value is higher than the time-averaged Nusselt number obtained for an isothermal sphere at the same Re=500 for forced convection flows (shown in Fig. 1b). In the case of the smoldering sphere, the transient evolution of the surface temperature creates a higher fluid-surface temperature gradient because of the lag in temperature evolution of surface adjacent fluid, which lead to a higher Nusselt number. We have observed that the obtained Nusselt number for the present mixed convection flow over the smoldering sphere does not follow any existing Nusselt number correlations as the existing correlations are based on the forced convection flows.

For a closer investigation of the wake plumes, Fig. 8 shows the Q-criterion of the mixed-convection flow at $\hat{t}=110$ (corresponding to Ri=0.94) from three different views (side, top, and back of the particle). In this figure, the two tunnel-shaped heat plumes are clear from the top and back views. These two non-interacting counter-rotating plumes form as a result of the spiral motions of the fluid particles adjacent to the sphere's surface at high Ri as shown in the schematic streamline figures (Fig. 8c, e).

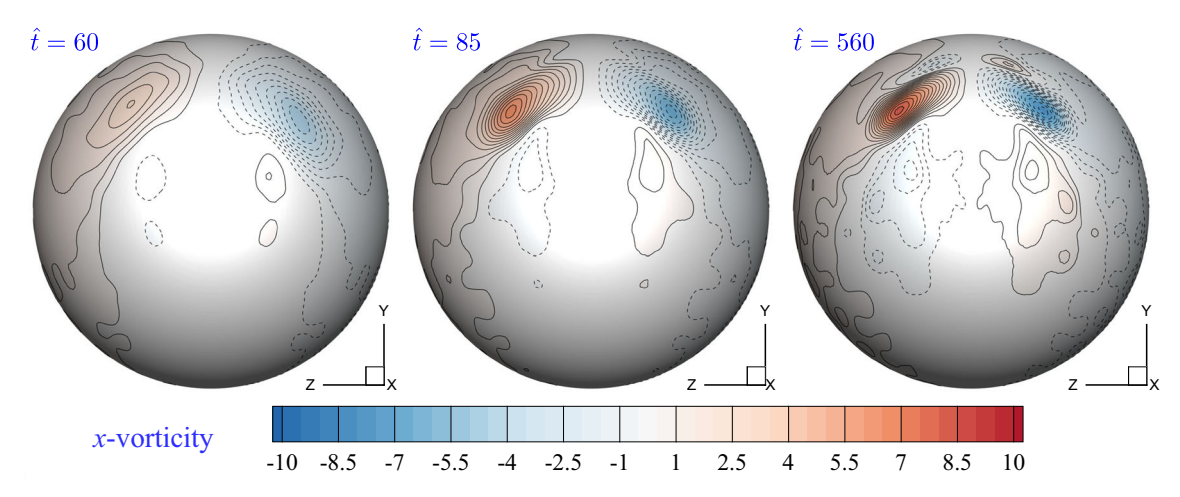


Fig. 9 x-vorticity footprint on the surface of the sphere viewed from the downstream direction. Solid and dotted lines represent positive and negative vorticities, respectively

The fluid particles next to the sphere's bottom surface heat up and glide upward, due to buoyancy, up to where the buoyancy and the inertial forces balance each other. As a result, the separation point shifts to the top half of the sphere (Fig. 8c). At the sphere's bottom surface, the velocity magnitude of the surface-adjacent fluid particles increases with the support of buoyancy and is proportional to the sphere's surface temperature, resulting in a decrease in pressure (discussed later; Fig. 12).

3.1.1 Surface vorticity

Figure 9 shows the footprint of the x-component of vorticities on the downstream half of the sphere at three instants of the simulation. Two dominating vortices are formed at $\hat{t}=60$, and the strength of the vortices gradually increases with time. The increase in the vortex strength is a consequence of the increase in the surface temperature of the sphere and the larger buoyancy force, which leads to an increase in upward fluid velocity in the downstream. The strength and center of the vortices remain relatively unchanged after $\hat{t}=360$ as there is no considerable change in the average surface temperature after this time. The persistent symmetry about the vertical (z-) plane in the vorticity plot is a result of the formation of the tunnel-shaped non-shedding wake plumes behind the sphere, which leads to non-fluctuating instantaneous drag and lift forces on the heated sphere (discussed below).

3.2 Drag and lift force analyses and firebrand trajectory

Figure 10a and b, respectively, show the instantaneous drag and lift coefficient variations throughout the smoldering process of the sphere. In these figures, the averaged drag and lift coefficient values for a nonheated sphere at Re = 500 are also shown. It is evident that the drag coefficient increases with the increase in the smoldering heat following the trend of the sphere's average surface temperature (Fig. 4), while the lift coefficient, C_L , (calculated based on Eq. 3) decreases to negative values. The negative lift force is a result of the buoyancy force that causes a higher velocity and thus a lower pressure at the lower half of the sphere as compared to the upper half. The instantaneous pressure coefficient variations along the z-plane of the sphere (refer to Fig. 6) are shown in Fig. 11. The instantaneous pressure coefficient variation over the smoldering sphere indicates that the pressure at the bottom half of the sphere continuously decreases with the increase in temperature. However, as opposed to the flow over a non-heated sphere, when Ri > 0.7, this instantaneous pressure represents symmetry about the vertical plane (not shown) on the downstream due to the presence of identical tunnel-shaped trailing vortices and the lack of vortex shedding phenomena (as shown in Figs. 8d and 9).

$$C_L = \frac{1}{\frac{1}{2}\rho U_{\infty}^2 A} \left(-\int_S p\mathbf{e_y} \cdot \mathbf{nd}S + \int_S \mathbf{n} \cdot \boldsymbol{\tau} \cdot \mathbf{e_y} \, dS \right)$$
(3)

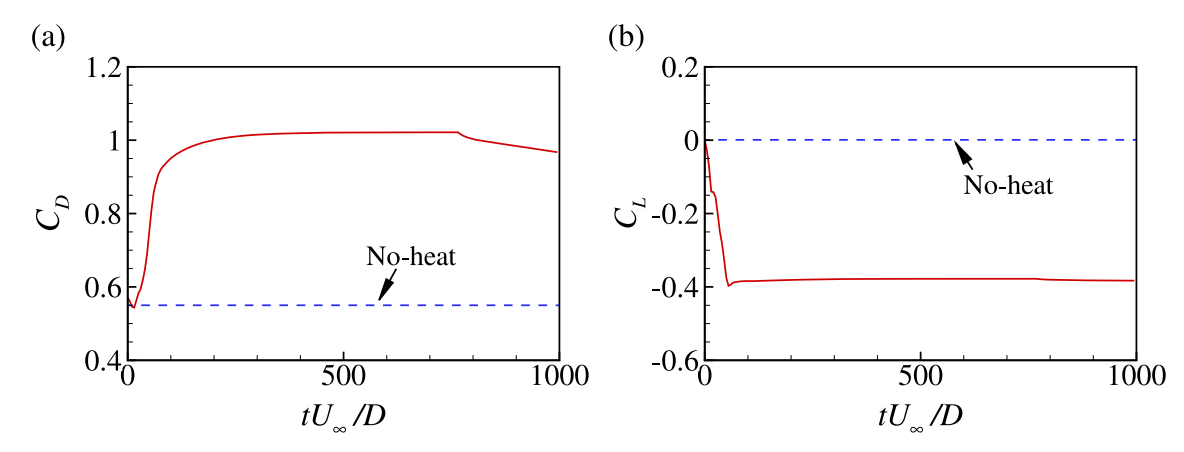


Fig. 10 Temporally varying a drag and b lift coefficients of an idealized smoldering firebrand

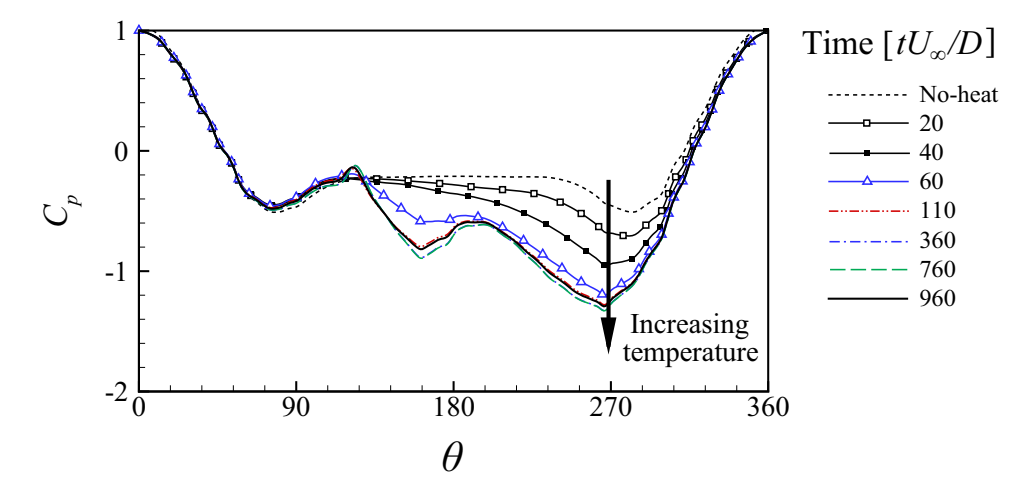


Fig. 11 The instantaneous pressure coefficient profile along the *z*-plane (refer to Fig. 6) on the surface of the smoldering sphere. The 90 and 270-degree points are, respectively, the top and bottom-most points of the sphere

The increase of the drag coefficient is also attributed to the buoyancy force as the increase in surface temperature causes higher upward flow velocities adjacent to the sphere surface at the downstream half of the sphere, resulting in a pressure drop at this location. The instantaneous pressure coefficient at the suction location (measured at 180 degrees from the front; $C_{p,b}$) quantifies the pressure drop with the increase in temperature at the downstream and is shown in Fig. 12. The pressure difference between the upstream and downstream of the sphere increases with the increase in temperature, which ultimately results in an increase in the drag force on the sphere.

In the following, we investigate how much error occurs if the transient evolution of temperature in the aerodynamics of a smoldering particle is not considered. For this, the difference in transient aerodynamic forces of a sphere with evolving surface temperature was compared to the steady state aerodynamic forces of an isothermal sphere with the same surface temperatures. In this analysis, six discrete temperature points between the T_{max} and T_{∞} , where T_{max} and T_{∞} are, respectively, the maximum average temperature of the sphere during the smoldering process and the ambient temperature, were considered. Figure 13 shows the drag and lift coefficients of the smoldering sphere, in solid red symbols, at instances when the average surface temperature ($T_{s,avg}$) of the sphere is equal to each of the six chosen discrete temperatures. Using the same six discrete surface temperatures, six separate flow simulations over isothermal spheres were performed and it was allowed the flow to reach a quasi-steady state. The quasi-steady state drag and lift coefficients of the isothermal spheres are shown in blue in Fig. 13, and the difference in the aerodynamic forces between the two sets of simulations is shown with shaded areas. It can be seen that the difference between the transient and quasi-steady state aerodynamic forces is maximum at the flow-developing stage of the simulations when the surface temperature of the sphere changes rapidly. The undeveloped flow patterns near the sphere surface for

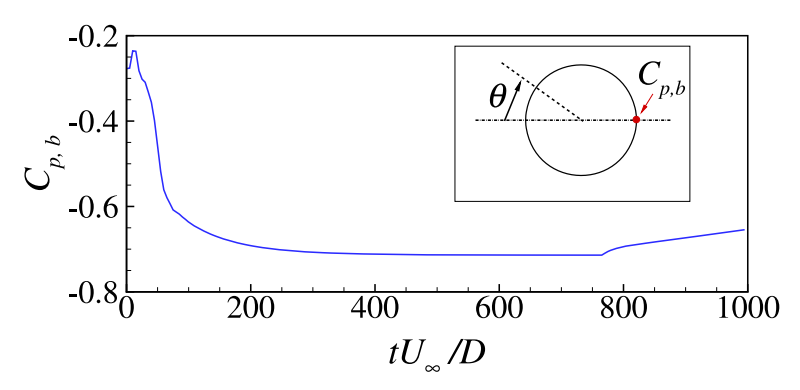


Fig. 12 Variation of the instantaneous pressure coefficient at the base (180 degrees from the front) of the smoldering sphere

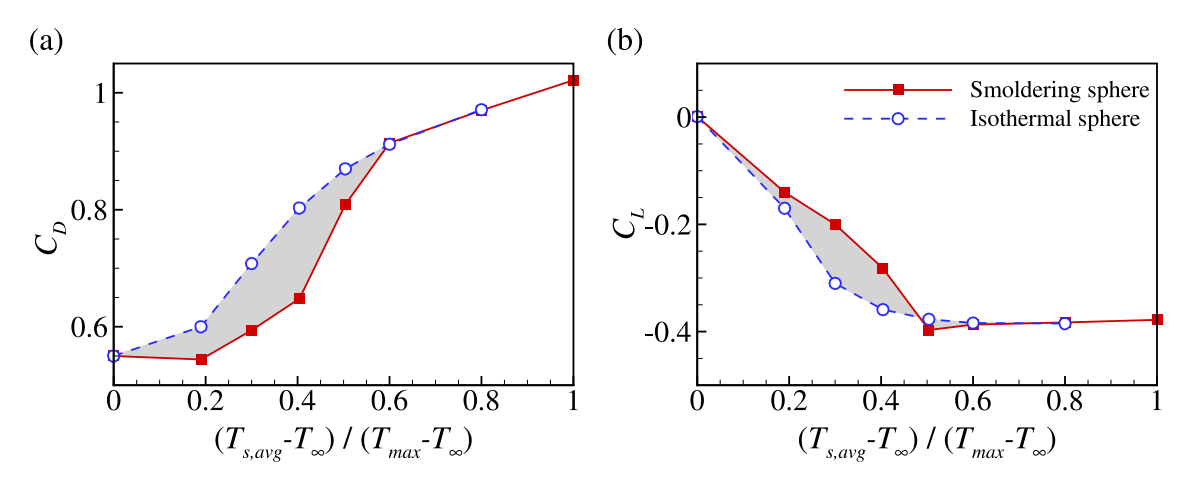


Fig. 13 Effect of the temporal evolution of smoldering temperature on the a drag and b lift coefficients of a spherical particle

the transient smoldering case cause a dissimilarity in aerodynamic force in comparison with the isothermal quasi-steady cases. Due to these differences in the aerodynamic forces, the assumption of an isothermal quasisteady state for smoldering particles may lead to inaccurate prediction of the particles' landing location. An example analysis of a firebrand trajectory is discussed in the next section.

3.2.1 Firebrand trajectory

The trajectory of firebrand particles is a function of the instantaneous drag and lift forces acting on them. Here, we investigate how the difference in the aerodynamic forces modify particle trajectories when comparing smoldering, non-heated, and isothermal particles of a fixed spherical shape. The results are also compared against those found using typical drag coefficient correlations for firebrands based only on the instantaneous Re following the formula reported in Tse & Fernandez [58] (Eq. 4) and Anthenien et al. [5] (Eq. 5).

$$C_D = \begin{cases} \frac{24}{Re} \left(1 + \frac{3Re}{16} \right)^{1/2}, & \text{for } Re \le 680\\ 0.4, & \text{for } 680 < Re \le 3 \times 10^5 \end{cases}$$

$$C_D = \frac{24}{Re} \left(1 + 0.15 \, Re^{0.687} \right) + \frac{0.42}{1 + 4.25 \times 10^4 Re^{-1.16}}, & \text{for } Re \le 3 \times 10^5$$
(5)

$$C_D = \frac{24}{Re} \left(1 + 0.15 \, Re^{0.687} \right) + \frac{0.42}{1 + 4.25 \times 10^4 \, Re^{-1.16}} \,, \quad \text{for Re} \le 3 \times 10^5$$
 (5)

It is assumed that the particles are released from a height of 40 m with an initial streamwise velocity of 3.12 m/s in a still flow, and therefore, only the vertical and horizontal forces are considered. The imbalance in forces acting on the particle results in particle acceleration, and Newton's law of motion govern this process according to:

$$m_p \frac{d\mathbf{V}_p}{dt} = \mathbf{F}_g + \mathbf{F}_D + \mathbf{F}_L \tag{6}$$

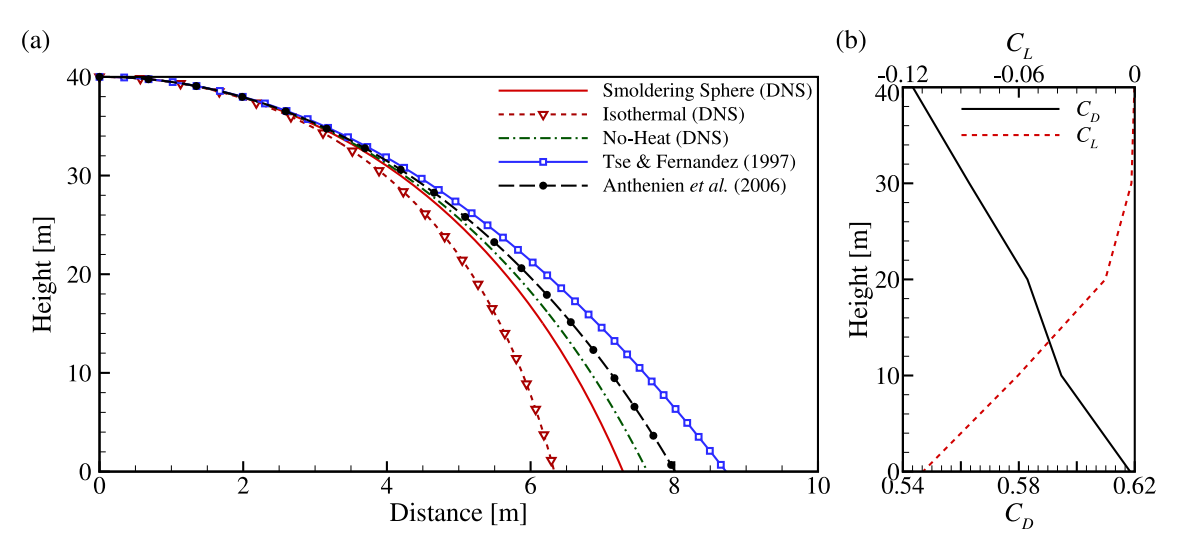


Fig. 14 a Projectile path of idealized firebrands under the influence of different drag and lift forces. b Corresponding lift and drag coefficient variations for the smoldering sphere

here $m_{\rm p}$ (kg) is the particle mass, $V_{\rm p}$ (m/s) is the particle's resultant velocity vector, and $F_{\rm g}$, $F_{\rm D}$, and $F_{\rm L}$, measured in newton (N), are, respectively, the gravitational, drag, and lift forces acting at the center of the sphere. For the smoldering particle, the drag and lift forces are based on the instantaneous drag and lift coefficients obtained above. The drag and lift forces are, respectively, based on Eqs. (7) and (8), in which ρ_{air} is the density of the air and A_p is the projected area of the sphere.

$$\mathbf{F}_{\mathrm{D}} = \frac{1}{2} C_D \, \rho_{air} \, A_p \, \left| \mathbf{V}_{\mathrm{p}} \right|^2 \, \frac{\mathbf{V}_{\mathrm{p}}}{\left| \mathbf{V}_{\mathrm{p}} \right|} \tag{7}$$

$$\mathbf{F}_{D} = \frac{1}{2} C_{D} \rho_{air} A_{p} \left| \mathbf{V}_{p} \right|^{2} \frac{\mathbf{V}_{p}}{\left| \mathbf{V}_{p} \right|}$$

$$\mathbf{F}_{L} = \frac{1}{2} C_{L} \rho_{air} A_{p} \left| \mathbf{V}_{p} \right|^{2} \frac{\mathbf{V}_{p}}{\left| \mathbf{V}_{p} \right|}$$

$$(8)$$

Figure 14a compares particle trajectories for the different cases. For all cases, the Re was set to 500 at the releasing point, and it was let to be found instantaneously based on the particle's instantaneous velocity. Figure 14a shows that particle trajectories found using the drag coefficient correlations in Eqs. (4) and (5) overpredict the spotting distance by, respectively, 19% and 10% compared to that found for the smoldering particle. It can also be seen that the isothermal and non-heated assumptions result in shorter and longer trajectories compared to the trajectory of the smoldering particle with differences of 13% and 4%, respectively, in the landing positions. The larger drag and more negative lift found for the isothermal and smoldering spheres justify their shorter trajectories and spotting distances compared to the other cases.

Figure 14b illustrates the variations in the drag (C_D) and lift (C_L) coefficients of the smoldering particle with respect to the particle's vertical position during its flight. While the drag coefficient of the smoldering particle varies between 0.55 and 0.62 and its lift coefficient varies between to -0.11 during its ~ 3 s flight time, $[C_D, C_L]$ of the isothermal and non-heated particles are [1.01, -0.379] and [0.55, 0.0], respectively. This is while the drag coefficients for the Tse & Fernandez [58] and Anthenien et al. [5] cases in the figure are calculated using Eqs. (4) and (5), respectively, based on the instantaneous particle velocity V_p The drag and lift coefficients for the isothermal sphere were obtained from the simulation of an isothermal sphere whose surface temperature was equal to the maximum average temperature (T_{max}) of the smoldering sphere.

It should be noted that the extent to which the particle undergoes the full spectrum of the smoldering heat variation, and consequently, traverses the entirety of the drag coefficient curve during its flight, depends on the particle flight time, which itself is defined by several factors, including the particle release condition, release height, and the background wind condition. The comparison performed in Fig. 14 was kept simple (i.e., using fixed particle release height and velocity with no background wind) to isolate the effect of the particle heating on the travel distance of the particles.

4 Conclusions

Using a computational framework that employs a one-way coupling between DNS and energy balance analysis, this study investigates the role of spatiotemporally variable surface temperatures over a spherical particle of a large Biot number on its aerodynamic behavior. The spatiotemporally variable surface temperature of the particle is a result of an internal transient smoldering heat source and the external variable velocity field over the surface of the particle. The study is inspired by the lack of information on the effect of transient temperatures on the aerodynamic forces and transport of particles, for which an important example is firebrand particles that smolder during their flight path and are the major component of wildfire propagation. While firebrand particles might go through shape and size changes as they smolder, in this study, it is assumed that the particle conserves its shape and only the effect of the unsteady smoldering heat on the aerodynamic forces is investigated.

Investigation of the wake flow over the idealized firebrand particle considered in this study revealed a very different flow behavior compared to that of non-heated particles. A noticeable characteristic of the wake flow is that, with the increase in particle's *Ri* and due to the buoyancy effects, the interlocked hairpin vortex structures seen behind non-heated spherical particles gradually vanish and merge into two well-defined non-interacting tunnel-shaped heat plumes. These two counter-rotating plumes form as a result of the spiral motions of the fluid particles next to the sphere's surface, and their vortex strength increases with the increase in the buoyancy force.

The results also indicate that the variations in the particle Ri and Nusselt numbers follow the variations in the particle smoldering heat input profile (that was unique for this study) and the resulting sphere surface temperature. Following the variations in the internal heat input profile, the Ri increases from small values until the flow develops to the mixed convection regime, while the increase in the Nusselt number indicates that the convection mode gradually dominates the conduction mode in the fluid as the sphere temperature increases. In addition, the instantaneous drag and lift coefficients are significantly dependent on the variations in the particle temperature. It is observed that the higher buoyancy-driven flow velocities adjacent to the surface cause a pressure drop on the downstream and bottom halves of the sphere. As a result, the sphere experiences larger drag and negative lift during its flight as the surface temperature increases, which results in a shorter flight compared to a non-smoldering sphere.

The results also show that the assumption of steady state (versus transient) temperatures for a particle with evolving temperature results in different aerodynamic force predictions. Due to the variations in the particle surface temperature, the undeveloped flow patterns near the sphere surface cause aerodynamic forces that are different than those of the developed flows of isothermal quasi-steady cases with the same instantaneous temperatures. It should be noted that, in the setup considered in this study, while the particle surface temperature varies spatiotemporally, the variations seen in the modified flow and aerodynamic forces are mainly due to the temporal (not spatial) variations of the temperature. That is because the instantaneous deviations in the non-uniform sphere surface temperature from the mean temperature are less than 10%, which is governed by the variations in the flow velocity and depends on the *Re*. Given this fact, we anticipate that under the current setup, a two-way coupling between the DNS and energy balance analysis would have negligible effect on the results found from the one-way coupling.

The findings of this study emphasize that neglecting the influence of transient thermal (and similarly, physical) conditions of particles may result in inaccurate particle trajectories and their landing spots as they affect the instantaneous drag and lift forces of particles. As seen in this study, the variations in the wake flow, aerodynamic forces, Ri, and Nusselt number strongly depend on the characteristics of the smoldering process and thus it is expected to be different for particles of different materials with different thermal properties. However, similar behavior as seen in this study is expected to occur if the smoldering process is predicted following the general trend of the heat release rate in the t2-fire growth model [18].

Acknowledgements This work is supported by funding from the Department of Defense Strategic Environmental Research and Development Program (SERDP) Grant Number RC20-1298 and National Science Foundation (NSF) Grant Number CBET 2043103. In addition, this research used resources of the National Energy Research Scientific Computing Center, a DOE Office of Science User Facility supported by the Office of Science of the U.S. Department of Energy under Contract No. DE-AC02-05CH11231 using NERSC award BER-ERCAP0022408. We would also like to acknowledge high-performance computing support from Cheyenne (doi:10.5065/D6RX99HX) provided by NCAR's Computational and Information Systems Laboratory, sponsored by the National Science Foundation.

Declarations

Conflict of interest The authors declare no competing interests.

Author contributions B.M.: Formal analysis, Investigation, Methodology, Software, Validation, Writing—original draft, Writing—review and editing. S.S.: Methodology, Software, Writing—review and editing. N.Y.: Conceptualization, Funding acquisition, Formal analysis, Investigation, Methodology, Supervision, Writing—original draft, Writing—review and editing.

Data availability The data that support the findings of this study will be available from the corresponding author upon reasonable request.

Appendix A: Model details and governing equations

The complex-environment temperature and moisture predictor (CeTMP) model details

The surface energy balance modeling in this work is performed using the CeTMP model [42] that is a coupled surface energy and moisture balance analysis model for simulating the spatiotemporal variations of temperature and moisture of complex objects/fuels in complex environments with variable conditions. To enable the simulations of complex terrains and objects, the model employs non-uniform triangular surface patches, each of which can consist of diverse material compositions and multiple material layers. The fundamental formula for the energy equilibrium at a triangular patch i (Eq. 9) includes: (1) net radiative heat exchanges ($R_{net,i}$ (W)) comprising of net shortwave ($R_{SW,net,i}$ (W)) and net longwave ($R_{LW,net,i}$ (W)) radiations absorbed over the patch, (2) convective heat exchanges at the patch surface including sensible ($Q_{H,i}$ (W)) and latent ($Q_{E,i}$ (W)) heat, and (3) conduction of heat ($Q_{G,i}$ (W)) normal to the patch material layers. In the presence of a heat source, a heat input ($Q_{E,i}$ (W)) is also considered.

$$R_{net,i} = Q_{G,i} + Q_{H,i} + Q_{E,i} + Q_{F,i}$$
(9)

Due to the Stefan–Boltzmann law that governs the longwave radiation, Eq. (9) is a fourth-order equation that is solved to determine the patch surface temperature (T_i) at each time step. Equation (9) is solved using the Newton–Raphson iteration method until the patch surface temperature varies less than 0.001 K between the successive iterations. The terms in the energy equilibrium equation are briefly explained below. For more details, we recommend referring to Saxena et al. [42].

Radiation

The net radiative exchanges occurring at each triangular patch are a combination of absorbed, reflected and/or emitted shortwave and longwave radiations given by the following equations:

$$R_{net,i} = R_{SW,net,i} + R_{LW,net,i} \tag{10}$$

$$R_{SW net i} = R_{SW i} \downarrow - R_{SW i} \uparrow \tag{11}$$

$$R_{LW,net,i} = R_{LW,i} \downarrow - R_{LW,i} \uparrow \tag{12}$$

where $R_{SW,i} \downarrow (W)$ and $R_{LW,i} \downarrow (W)$ are the total downwelling shortwave and longwave radiation received by the patch, while $R_{SW,i} \uparrow (W)$ and $R_{LW,i} \uparrow (W)$ are the total upwelling shortwave and longwave radiation reflected by the patch.

Convective heat transfer

The sensible heat flux occurring between the surface patch and the atmosphere is determined based on the following equation:

$$Q_{H,i} = h_i \left(T_i - T_{air} \right) A_i \tag{13}$$

where the convection coefficient (h_i) is determined based on the McAdams [26,36] convective coefficient correlation (i.e., $h_i = 5.7 + 3.8V_z$, with V_z being the velocity magnitude adjacent to the each triangular surface patch). Among the different methods for calculating the convection coefficient in CeTMP, this method was chosen for this study since it can be applied to surfaces with any orientation and roughness and also includes the natural convection part of the total convection coefficient.

Conductive heat flux

Conduction through the substrate layer of each patch is estimated using a finite difference method (FDM) that employs the Crank-Nicholson time-stepping scheme according to:

$$T_{L}^{t+1} - T_{L}^{t} = \frac{\Delta t}{\rho_{L} C_{L} \Delta z_{L}} \left[\frac{1}{2} \left(G_{L-1,L}^{t+1} - G_{L,L+1}^{t+1} \right) + \frac{1}{2} \left(G_{L-1,L}^{t} - G_{L,L+1}^{t} \right) \right]$$
(14)

$$G_{L-1,L}^{t} = k_{L-1,L} \frac{(T_{L-1}^{t} - T_{L}^{t})}{\frac{1}{2}(\Delta z_{L-1} + \Delta z_{L})}$$
(15)

here T_L (K), Δz_L (m), ρ_L (kg m⁻³), and C_L (J kg¹ K ¹) are, respectively, the temperature, thickness, density, and specific heat capacity of material layer L. $G_{L-1,L}^t$ (W m⁻²) is the conductive heat flux between layers L-1 and L at timestep t, where $k_{L-1,L}$ (W m¹ K¹) is the conductivity between layers L-1 and L. Temperatures (T_L (K)) of the material layers (L from 1 to the deepest layer) are solved at each time step for each triangular patch. Then, the patch surface temperature at the next time step (T_i^{t+1}) is solved using the energy balance equation (Eq. 9), where the conduction term for the FDM is given by Eq. (16). The inner extreme of the patch substrate is bounded by an internal temperature that is imposed/simulated depending on the physics under investigation. In this study, the internal object temperature varies according to the t2fire growth model, representing the heat release rates of typical burning items versus time (see below)

$$Q_{G,i} = -k_1 A_i \frac{(T_i^{t+1} - T_1^t)}{0.5\Delta z_1} \tag{16}$$

In Eq. (16), k_1 (W m⁻¹ K⁻¹), T_1^t (K), and Δz_1 (m), are, respectively, the conductivity, temperature, and thickness of the first material layer below the surface, and A_i (m²) is the surface area of patch under consideration.

t2-fire growth model

The t2 fire growth model for defining the internal heat input is given by the following formulations:

$$Q_{F,i} = \alpha_f (t - t_o)^2 \quad t_o \le t \le t_{lo} Q_{F,i} = \alpha_f (t_{lo} - t_o)^2 \quad t_{lo} \le t \le t_d \alpha_d (t_{end} - t)^2 \quad t_d \le t \le t_{end}$$
(17)

here α_f is a fire growth coefficient, α_d is a fire decay coefficient, t_o is the time to onset of ignition, t_{lo} is the level-off time, t_d marks the time at which decay begins, and t_{end} denotes time when the internal heating process is terminated. More details about this model can be found in [18].

Governing equations for the DNS model

The governing equations for the fluid flow field are the non-dimensional incompressible Navier–Stokes equations with the Boussinesq approximation,

$$\nabla \mathbf{u} = 0 \tag{18}$$

$$\frac{\partial \mathbf{u}}{\partial t} + \nabla \left(\mathbf{u}\mathbf{u}\right) = -\nabla p + \frac{1}{Re} \nabla^2 \mathbf{u} + Ri\Theta \tag{19}$$

$$\frac{\partial \Theta}{\partial t} + \mathbf{u} \nabla \Theta = \frac{1}{RePr} \nabla^2 \Theta \tag{20}$$

In these equations, $\mathbf{u}(\mathbf{x},t)$ is the fluid velocity with \mathbf{x} and t representing the location vector and time, p is the dynamic pressure, Θ is the non-dimensional temperature defined as $\Theta = (T - T_{\infty})/(T_{max} - T_{\infty})$ with T, T_{∞} , and T_{max} being the instantaneous temperature, free-stream temperature and maximum average temperature of the sphere during the smoldering process $Re = U_{\infty}D/v$ is the Reynolds number, $Pr = v/\alpha$ is the Prandtl number, and $Ri = g\beta\Delta TD/U_{\infty}^2$ is the Richardson number. v is the kinematic viscosity, D is characteristic length scale, U_{∞} is the free-stream velocity, α is the thermal diffusivity of the fluid, g is the gravitational

constant, β is the coefficient of thermal expansion, and ΔT is the difference between the spatially averaged surface temperature of the sphere at an instant $(T_{s,avg})$ and the free-stream temperature (T_{∞}) .

The one-way coupling between the DNS and CeTMP model was through handling the thermal boundary condition for the flow phase. In this process, the wind velocity local to each patch was first found from DNS of the flow past a non-heated sphere at the selected Re (= 500) then provided to the convection heat transfer coefficient equation (h_i) to find convective heat transfer exchanges (Eq. 13) in the energy balance analysis. The simulated surface temperature of each patch (T_i) in CeTMP was then provided to Eqs. (19) and (20) as a boundary condition for each triangular mesh element of the immersed boundary surface at each time step of the simulation. This process allows for setting a spatiotemporally variable Dirichlet thermal boundary condition over the sphere.

Appendix B: Domain and grid sensitivity analyses

Table 2 below presents the results of our domain sensitivity analysis conducted using three different domain sizes (Dom A, Dom B, and Dom C) at Re = 500. To ensure a convergence in this sensitivity analysis, the time-averaged drag coefficient of the sphere served as the error metric. The percentage change in the drag coefficient due to variations in the domain size is reported in the last column of the table. The minimum grid spacing (Δ_{min}) near the sphere surface was kept constant for all the three domain sizes. These analyses indicated that the first increment in the domain size from Dom A to Dom B led to a 2.17% change in the C_D , while the second increment from Dom B to Dom C resulted in a small change of 0.96% in C_D . It should be noted that, however, the computational expenses significantly increased with the second domain size increment, leading to the selection of Dom B for further analysis.

Table 2 Influence of the grid resolution on the drag coefficient

Domain	Domain size	Grid number	$\Delta_{ ext{min}}$	Mean C_D	% change in C_D
Dom A	$20D \times 8D \times 8D$	236 × 189 × 189	0.005	0.5621	
Dom B	$24D \times 10D \times 10D$	248 × 197 × 197	0.005	0.5499	
Dom C	$26D \times 16D \times 16D$	254 × 217 × 217	0.005	0.5446	

Table 3 Influence of the domain size on the drag coefficient

Grid	Grid number	$\Delta_{\mathbf{min}}$	Mean C_D	% change in C_D
Grid A	$220 \times 140 \times 140$	0.0078	0.5406	_
Grid B	$248 \times 197 \times 197$	0.005	0.5499	1.72
Grid C	$273 \times 251 \times 251$	0.0031	0.5551	0.95

A grid sensitivity analysis was performed using Dom B to ensure the accuracy of the results. Three different grid resolutions (Grid A, Grid B, and Grid C) were considered as detailed in Table 3. The considerably small error in the estimation of the drag coefficient between Grid B and Grid C resolutions indicates that Grid B is fine enough to accurately capture the flow dynamics of the present problem. Given the large computational expenses of the finest grid setup (Grid C), Grid B was chosen for the present analysis.

References

- 1. Achenbach, E.: Vortex shedding from spheres. J. Fluid Mech. 62(2), 209–221 (1974)
- 2. Albini, F.A.: Spot Fire Distance from Burning Trees: A Predictive Model, vol. 56. Intermountain Forest and Range Experiment Station, Forest Service, US Department of Agriculture (1979)
- 3. Albini, F.A.: Spot Fire Distance from Isolated Sources: Extensions of A Predictive Model, vol. 309. US Department of Agriculture, Forest Service, Intermountain Forest & Range Experiment Station (1981)
- 4. Albini, F.A.: Potential Spotting Distance from Wind-driven Surface Fires, vol. 309. US Department of Agriculture, Forest Service, Intermountain Forest & Range Experiment Station (1983)

- 5. Anthenien, R.A., Stephen, D.T., Fernandez-Pello, A.C.: On the trajectories of embers initially elevated or lofted by small scale ground fire plumes in high winds. Fire Saf. J. 41(5), 349–363 (2006)
- 6. Bagchi, P., Ha, M.Y., Balachandar, S.: Direct numerical simulation of flow and heat transfer from a sphere in a uniform cross-flow. J. Fluids Eng. 123(2), 347–358 (2001)
- 7. Baranovskiy, N.V., Malinin, A.: Mathematical simulation of forest fire front influence on wood-based building using one-dimensional model of heat transfer. In: E3S Web of Conferences, vol. 200, p. 03007. EDP Sciences (2020)
- 8. Batchelor, G.K.: An Introduction to Fluid Dynamics. Cambridge University Press, Cambridge (2000)
- 9. Bhutia, S., Ann Jenkins, M., Sun, R.: Comparison of firebrand propagation prediction by a plume model and a coupled-fire/atmosphere large-eddy simulator. J. Adv. Model. Earth Syst. (2010). https://doi.org/10.3894/JAMES.2010.2.4
- 10. Burmeister, L.C.: Convective Heat Transfer. Wiley, New Jersey (1993)
- 11. Chorin, A.J.: On the convergence of discrete approximations to the Navier-Stokes equations. Math. Comput. **23**(106), 341–353 (1969)
- 12. Clift, R., Gauvin, W.: Motion of entrained particles in gas streams. Can. J. Chem. Eng. 49(4), 439-448 (1971)
- 13. Dong, H., Bozkurttas, M., Mittal, R., Madden, P., Lauder, G.: Computational modelling and analysis of the hydrodynamics of a highly deformable fish pectoral fin. J. Fluid Mech. **645**, 345–373 (2010)
- 14. Ganguli, S., Lele, S.K.: Drag of a heated sphere at low Reynolds numbers in the absence of buoyancy. J. Fluid Mech. **869**, 264–291 (2019)
- 15. Grishin, A.M.: Mathematical Modeling of Forest Fires and New Methods of Fighting Them. Publishing House of the Tomsk State University, Tomsk (1997)
- 16. Johnson, T.A., Patel, V.C.: Flow past a sphere up to a Reynolds number of 300. J. Fluid Mech. 378, 19–70 (1999)
- 17. Kim, H.J., Durbin, P.A.: Observations of the frequencies in a sphere wake and of drag increase by acoustic excitation. Phys. Fluids **31**(11), 3260–3265 (1988)
- 18. Kim, H.-J., Lilley, D.G.: Heat release rates of burning items in fires. J. Propul. Power 18(4), 866–870 (2002)
- 19. Koo, E., Linn, R.R., Pagni, P.J., Edminster, C.B.: Modelling firebrand transport in wildfires using HIGRAD/FIRETEC. Int. J. Wildland Fire 21(4), 396–417 (2012)
- 20. Kramers, H.: Heat transfer from spheres to flowing media. Physica 12(2-3), 61-80 (1946)
- 21. Kurose, R., Anami, M., Fujita, A., Komori, S.: Numerical simulation of flow past a heated/cooled sphere. J. Fluid Mech. 692, 332–346 (2012)
- 22. Lapple, C.E.: Particle dynamics (1951)
- 23. Manzello, S.L., Foote, E.I.: Characterizing firebrand exposure from wildland-urban interface (WUI) fires: results from the 2007 Angora Fire. Fire Technol. **50**(1), 105–124 (2014)
- Manzello, S.L., Suzuki, S., Gollner, M.J., Fernandez-Pello, A.C.: Role of firebrand combustion in large outdoor fire spread. Prog. Energy Combust. Sci. 76, 100801 (2020)
- 25. Maranghides, A., Mell, W.: A case study of a community affected by the Witch and Guejito wildland fires. Fire Technol. 47(2), 379–420 (2011)
- 26. McAdams, W.H.: Heat Transmission, vol. 3. McGraw-Hill Kogakusha, Tokyo (1954)
- 27. Mell, W.E., Manzello, S.L., Maranghides, A., Butry, D., Rehm, R.G.: The wildland-urban interface fire problem-current approaches and research needs. Int. J. Wildland Fire 19(2), 238–251 (2010)
- 28. Mindykowski, P., Fuentes, A., Consalvi, J., Porterie, B.: Piloted ignition of wildland fuels. Fire Saf. J. 46(1-2), 34-40 (2011)
- 29. Mittal, R.: Planar symmetry in the unsteady wake of a sphere. AIAA J. 37(3), 388-390 (1999)
- 30. Mittal, R., Dong, H., Bozkurttas, M., Najjar, F.M., Vargas, A., von Loebbecke, A.: A versatile sharp interface immersed boundary method for incompressible flows with complex boundaries. J. Comput. Phys. 227, 4825–4852 (2008)
- 31. Musong, S.G., Feng, Z.G.: Mixed convective heat transfer from a heated sphere at an arbitrary incident flow angle in laminar flows. Int. J. Heat Mass Transf. 78, 34–44 (2014)
- 32. Nagata, T., Nonomura, T., Takahashi, S.: Direct numerical simulation of flow past a sphere at a Reynolds number between 500 and 1000 in compressible flows. In: 2018 AIAA Aerospace Sciences Meeting, p. 0381. American Institute of Aeronautics and Astronautics Inc, AIAA (2018)
- 33. NICC: Wildland Fire Summary and Statistics Annual Report, National Interagency Coordination Center (2022)
- 34. Ohmiya, Y., Iwami, T.: An investigation on the distribution of fire brands and spot fires due to a hotel fire. Fire Sci. Technol. **20**(1), 27–35 (2000)
- 35. Oppenheimer, N., Navardi, S., Stone, H.A.: Motion of a hot particle in viscous fluids. Phys. Rev. Fluids 1(1), 014001 (2016)
- 36. Palyvos, J.: A survey of wind convection coefficient correlations for building envelope energy systems' modeling. Appl. Therm. Eng. **28**(8–9), 801–808 (2008)
- 37. Pereira, J.C., Pereira, J., Leite, A.L., Albuquerque, D.: Calculation of spotting particles maximum distance in idealised forest fire scenarios. J. Combust. **2015**, 513576 (2015)
- 38. Ploumhans, P., Winckelmans, G., Salmon, J.K., Leonard, A., Warren, M.: Vortex methods for direct numerical simulation of three-dimensional bluff body flows: application to the sphere at Re= 300, 500, and 1000. J. Comput. Phys. 178(2), 427–463 (2002)
- 39. Pope, S.B.: Turbulent Flows. Cambridge University Press, Cambridge (2000)
- 40. Richter, A., Nikrityuk, P.A.: Drag forces and heat transfer coefficients for spherical, cuboidal and ellipsoidal particles in cross flow at sub-critical Reynolds numbers. Int. J. Heat Mass Transf. **55**(4), 1343–1354 (2012)
- 41. Rivera, J., Hernández, N., Consalvi, J., Reszka, P., Contreras, J., Fuentes, A.: Ignition of wildland fuels by idealized firebrands. Fire Saf. J. 120, 103036 (2021)
- 42. Saxena, S., Dubey, R.R., Yaghoobian, N.: A planning model for predicting ignition potential of complex fuels in diurnally variable environments. Fire Technol. **59**(5), 2787–2827 (2023)
- 43. Schiller, L., Nauman, A.Z.: A drag coefficient correlation. Zeit. Ver. Deutsch. Ing. 77, 318–320 (1933)
- 44. Schlichting, H., Kestin, J.: Boundary Layer Theory, vol. 121. Springer, New York (1961)
- 45. Shinohara, M., Sugii, K., Hosokawa, M.: The influence of characteristics of firebrands on the flight distance–based on the field survey of the city fire under the strong wind in Beppu-city, Oita (2010)

- 46. Shoele, K., Mittal, R.: Computational study of flow-induced vibration of a reed in a channel and effect on convective heat transfer. Phys. Fluids **26**(12), 127103 (2014)
- 47. Song, J., Huang, X., Liu, N., Li, H., Zhang, L.: The wind effect on the transport and burning of firebrands. Fire Technol. 53, 1555–1568 (2017)
- 48. Storey, M.A., Price, O.F., Sharples, J.J., Bradstock, R.A.: Drivers of long-distance spotting during wildfires in south-eastern Australia. Int. J. Wildland Fire **29**(6), 459–472 (2020)
- 49. Suzuki, S.: Study on characteristics of firebrands collected from three different fires. Rep. Natl. Res. Inst. Fire Disaster 123, 1–9 (2017)
- 50. Tarifa, C.S., Del Notario, P.P., Moreno, F.G.: On the flight paths and lifetimes of burning particles of wood. In: Symposium (International) on Combustion, vol. 10, pp. 1021–1037. Elsevier (1965)
- 51. Tarifa, C.S., Del Notario, P.P., Moreno, F.G., Villa, A.R.: Transport and Combustion of Firebrands. Final Report of Grants FG-SP-114 and FG-SP-146, vol. II (1967)
- 52. Terfous, A., Hazzab, A., Ghenaim, A.: Predicting the drag coefficient and settling velocity of spherical particles. Powder Technol. 239, 12–20 (2013)
- 53. Thomas, J.C., Mueller, E.V., Santamaria, S., Gallagher, M., El Houssami, M., Filkov, A., Clark, K., Skowronski, N., Hadden, R.M., Mell, W., et al.: Investigation of firebrand generation from an experimental fire: development of a reliable data collection methodology. Fire Saf. J. 91, 864–871 (2017)
- 54. Thompson, M.C., Leweke, T., Provansal, M.: Kinematics and dynamics of sphere wake transition. J. Fluids Struct. **15**(3–4), 575–585 (2001)
- Tohidi, A., Kaye, N.B.: Aerodynamic characterization of rod-like debris with application to firebrand transport. J. Wind Eng. Ind. Aerodyn. 168, 297–311 (2017)
- 56. Tohidi, A., Kaye, N.B.: Stochastic modeling of firebrand shower scenarios. Fire Saf. J. 91, 91–102 (2017)
- 57. Tomboulides, A.G., Orszag, S.A.: Numerical investigation of transitional and weak turbulent flow past a sphere. J. Fluid Mech. 416, 45–73 (2000)
- 58. Tse, S.D., Fernandez-Pello, A.C.: On the flight paths of metal particles and embers generated by power lines in high winds–a potential source of wildland fires. Fire Saf. J. 30(4), 333–356 (1998)
- 59. Urban, J.L., Song, J., Santamaria, S., Fernandez-Pello, C.: Ignition of a spot smolder in a moist fuel bed by a firebrand. Fire Saf. J. 108, 102833 (2019)
- Van Kan, J.: A second-order accurate pressure-correction scheme for viscous incompressible flow. J. Sci. Stat. Comput. 7(3), 870–891 (1986)
- 61. Vedula, V., Fortini, S., Seo, J.-H., Querzoli, G., Mittal, R.: Computational modeling and validation of intraventricular flow in a simple model of the left ventricle. Theoret. Comput. Fluid Dyn. 28(6), 589–604 (2014)
- 62. Vodvarka, F. J.: Firebrand Field Studies-Final Report. IIT Research Institute (1969)
- 63. Wang, Y., Wang, H., Jin, H., Guo, L.: Numerical simulation of adiabatic/cooled/heated spherical particles with Stefan flow in supercritical water. Phys. Fluids 33(5), 053305 (2021)
- 64. Ye, T., Mittal, R., Udaykumar, H., Shyy, W.: An accurate cartesian grid method for viscous incompressible flows with complex immersed boundaries. J. Comput. Phys. **156**(2), 209–240 (1999)
- 65. Yuge, T.: Experiments on heat transfer from spheres including combined natural and forced convection. J. Heat Transf. 82 (1960)
- Zang, Y., Street, R.L., Koseff, J.R.: A non-staggered grid, fractional step method for time-dependent incompressible Navier-Stokes equations in curvilinear coordinates. J. Comput. Phys. 114(1), 18–33 (1994)
- 67. Zheng, L., Hedrick, T.L., Mittal, R.: A multi-fidelity modelling approach for evaluation and optimization of wing stroke aerodynamics in flapping flight. J. Fluid Mech. **721**, 118–154 (2013)

Publisher's Note Springer Nature remains neutral with regard to jurisdictional claims in published maps and institutional affiliations.

Springer Nature or its licensor (e.g. a society or other partner) holds exclusive rights to this article under a publishing agreement with the author(s) or other rightsholder(s); author self-archiving of the accepted manuscript version of this article is solely governed by the terms of such publishing agreement and applicable law.